# 1 BAT data analysis and fitting

GRB 101225A was detected by BAT on-board the *Swift* satellite [23] on Dec. 25, 2010 at $T_0 = 18$:37:45 UT as an image trigger [24]. It was already in progress both when the source entered the BAT field of view and when it left the field of view due to *Swift* orbit-constrained slews [25, 26]. Therefore, we can only give lower limits on the total burst fluence and the T_{90} duration. The total fluence of the intervals covered in the observations adds up to $(5.6 \pm 0.7) \times 10^{-6}$ erg cm^{-2} (implying a total energy release in γ-rays of $E_{\gamma,iso} > 1.4 \times 10^{51}$ erg at $z = 0.33$.), which is a lower limit to the total gamma-ray emission. No emission was detected in a previous observation of the field at $T - T_0 = -4950$ s and we therefore put a lower limit on the duration of $T_{90} > 2000$ s. This is one of the highest durations ever observed for a GRB, comparable to the longest burst observed by *Swift*, GRB 090417B [27]. The BAT light curve is shown in SI Fig. 1. The BAT-observed peak flux of $(3.25 \pm 0.47) \times 10^{-9}$ erg cm^{-2} s^{-1} in the $15 - 150$ keV range occurred in the interval $T - T_0 = +1372$ to $T - T_0 = +1672$ s. No other γ-ray instrument detected GRB 101225A, although the MAXI instrument on board the ISS ($2-10$ keV) reported a marginal detection at $T - T_0 = +1002$ s coincident with the BAT position [28].

The time-averaged spectra from T_0 to $T - T_0 = +963$ s and from $T - T_0 = +1372$ to $T - T_0 = +1672$ s are best fit by simple power-law models with photon indices of $\Gamma = 1.9 \pm 0.4$ and 1.9 ± 0.2, respectively. The total fluences in each time period in the $15 - 150$ keV band taking these fits are $(1.7 \pm 0.4) \times 10^{-6}$ and $(9.0 \pm 0.2) \times 10^{-7}$ erg cm^{-2}. All quoted errors are at the 90% confidence level. The BAT spectra are almost equally well parametrised by models using a cutoff power-law or a black body fit due to the low signal-to-noise ratio of the event. E_{peak} using a cutoff model is poorly constrained to 38 ± 20 keV. The black body fit gives a temperature of kT= 10.1 ± 1.1 keV. Errors are at the 68% confidence level.

We also examined the BAT data to search for persistent emission after the trigger. For this we used the daily sky image mosaics produced as part of the BAT hard X-ray transient monitor which cover a single energy band of $15 - 50$ keV. We found a 5.3σ excess (0.0048 ± 0.0009 count cm^{-2} s^{-1}) on Dec. 25, 2010 (MJD 55555), the day of the trigger, and a positive excess in the count rate ($\geq 1\sigma$ or 0.0011 count cm^{-2} s^{-1}) over the next ten days (until MJD 55565). We determine the probability that such a sequence of excess rates would occur by chance. To do this, we examine the light curves of 106 "blank sky" points tracked in the BAT transient monitor. These are points chosen randomly across the sky at least 10 arcmin from any known X-ray source. Any positive flux from these points is expected to be due to chance fluctuations. In these 106 light curves ($> 200,000$ data points), we find only one sequence of six consecutive days showing a positive excess and none with more than six days. The chance probability of ten days of excess flux is less than 1/200,000, so the observed prolonged emission is likely real.
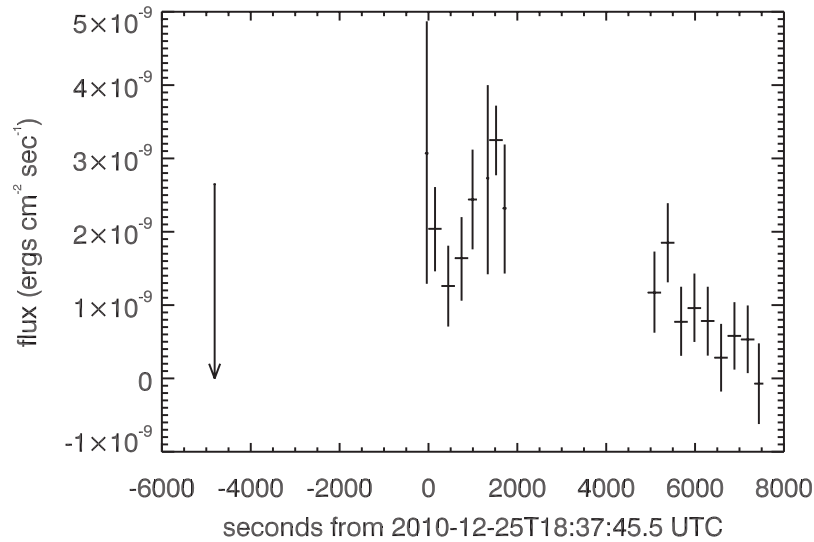
Supplementary Figure 1 | BAT γ-ray lightcurve in the 15-150 keV band. The sum of the flux was obtained using a fixed power-law index of $\Gamma = 1.87$ from a fit to the most intense part of the burst. The burst started before the beginning of the BAT data at $\sim T - T_0 = -100\,\text{s}$ and probably continued while the source was not in the BAT field of view from $T - T_0 = +1091$ to $T - T_0 = +1372\,\text{s}$. The latest upper limit before the burst was 2.65×10^{-9} erg cm^{-2} s^{-1} at $T - T_0 = -4950\,\text{s}$. Error bars are at 90% confidence.

2 XRT data analysis and fitting

The *Swift* XRT data were processed with version 3.7 of the XRT data reduction software (released as part of `HEASoft 6.10` on 2010-09-28), and the corresponding calibration files were used for subsequent spectral analysis. The object was detected by XRT from 1.4 ks to 10^5 s after the trigger. Data were collected in Windowed Timing (WT) mode for the first 7.3 ks after the trigger followed by Photon Counting (PC) mode for the rest of the observations. The peak flux in X-rays is 4.3×10^{-9} erg cm^{-2} s^{-1}, the total observed fluence 8.2×10^{-6} erg cm^{-2} and the unabsorbed fluence 1.1×10^{-5} erg cm^{-2}. At $z = 0.33$ this corresponds to a total energy release in X-rays of 3.6×10^{51} erg. Spectra were extracted for individual snapshots of data (one snapshot corresponds roughly to one orbit constrained by the observability of the object during the orbit) and were further timesliced into 100 s bins for the initial snapshot ($1.4 - 1.8\,\text{ks}$ after the trigger).

We tried a variety of fits to the X-ray data, using `XSPEC version 12.6.0`, with the result that an absorbed power-law plus black body component provided a good fit to the data (see SI Fig. 2). For the fit we used the Tübingen-Boulder absorption model with the Wilms abundances [29] and Verner absorption cross-section [30]. As shown in SI Fig. 3, there is little spectral evolution within the first snapshot of data. The best fit taking the entire first 367 s of data is a power-law with a photon index $\Gamma = 1.83^{+0.13}_{-0.10}$, a black body of temperature 0.96 ± 0.13 keV (1.11×10^7 K) and a total absorbing column of $(2.2 \pm 0.3) \times 10^{21}$ cm^{-2}, for a χ^2 of 420.7 for 379 degrees of freedom. The Galactic column density in this direction is 7.9×10^{20} cm^{-2}.

The inclusion of the black body is significant at the $> 99.9999\%$ level, the contribution of the black body to the total emission is around 20% (see SI Fig. 3). The second snapshot of data (also in WT mode) is again better fit with a black body in addition to the power-law, with $\Gamma = 2.18^{+0.12}_{-0.09}$, black body $kT = 0.99^{+0.15}_{-0.17}$ keV and NH $= (2.7 \pm 0.2) \times 10^{21}$ cm^{-2}, with χ^2/d.o.f $= 378/421$. This black body is significant at 99.987%. For the X-ray
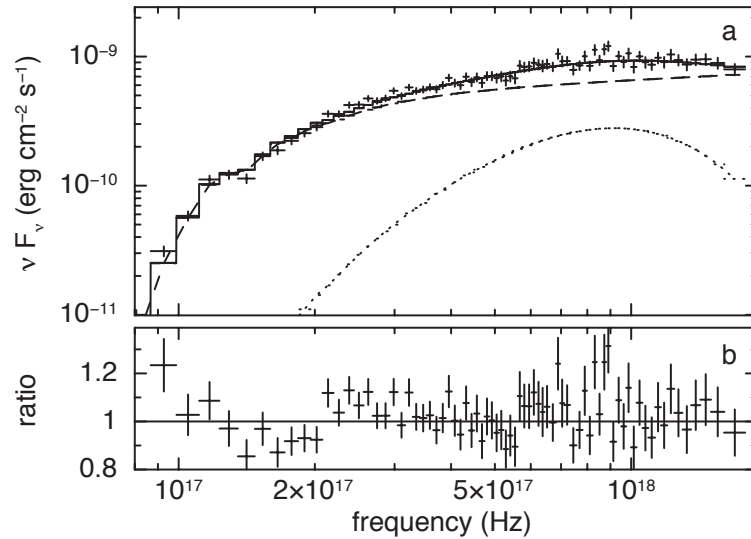
Supplementary Figure 2 | Fit to the X-ray spectrum. a: X-ray spectrum from XRT during the first snapshot. The solid line is the spectral fit, the dashed line indicates the contribution of the power-law component, the dotted line the contribution of the black body component. **b**: Ratio between the observed data and the fitted model.

data after the second snapshot, no black body component is required and a simple absorbed power-law provides an acceptable fit, likely due to the lower signal-to-noise ratio at later times.

| Model	Γ	kT (keV)	N_H (10^{22} cm^{-2})	χ^2/d.o.f. (F-test)
PL	1.72±0.03		0.24±0.02	468/381
PL+BB	$1.83^{+0.13}_{-0.10}$	0.96±0.13	0.22±0.03	421/379 (1.95×10^{-9})
PL+diskBB	$1.79^{+0.36}_{-0.22}$	1.64±0.35	0.18±0.04	417/379 (3.19×10^{-10})
PL+compt	1.79±0.04	<22	$0.31^{+0.03}_{-0.02}$	424/377 (1.55×10^{-7})

Supplementary Table 1 | Result of different model fits to the X-ray data of the first snapshot. PL is a pure power-law model, PL+black body (BB) a combination of a simple PL and a black body with one temperature while a PL+diskBB includes emission from black bodys with different temperatures, PL+compt includes a comptonized component in addition to the power-law. Γ is the photon index of the power-law, kT the black body temperature, the column density is the total density, including the Galactic absorption. The last column shows the χ^2 of the different fits and the F-test value compared to the simple absorbed PL model.

The detection of N_H in excess of the Galactic column density can be used to constrain the redshift since column density and redshift are coupled. We fitted the spectrum of the first orbit fixing the Galactic absorption to 7.93×10^{20} cm^{-2}. In addition to the absorbed powerlaw plus black body component as described above we allowed for a third component leaving both the column density and the redshift free to vary (in contrast to the fit described above where the redshift was fixed to 0.3). The resulting contours are plotted in SI Fig. 4. The 99% upper limit for the redshift is 0.5, the 90% upper limit on the redshift is 0.35, consistent with our findings from the UVOIR SED fitting.
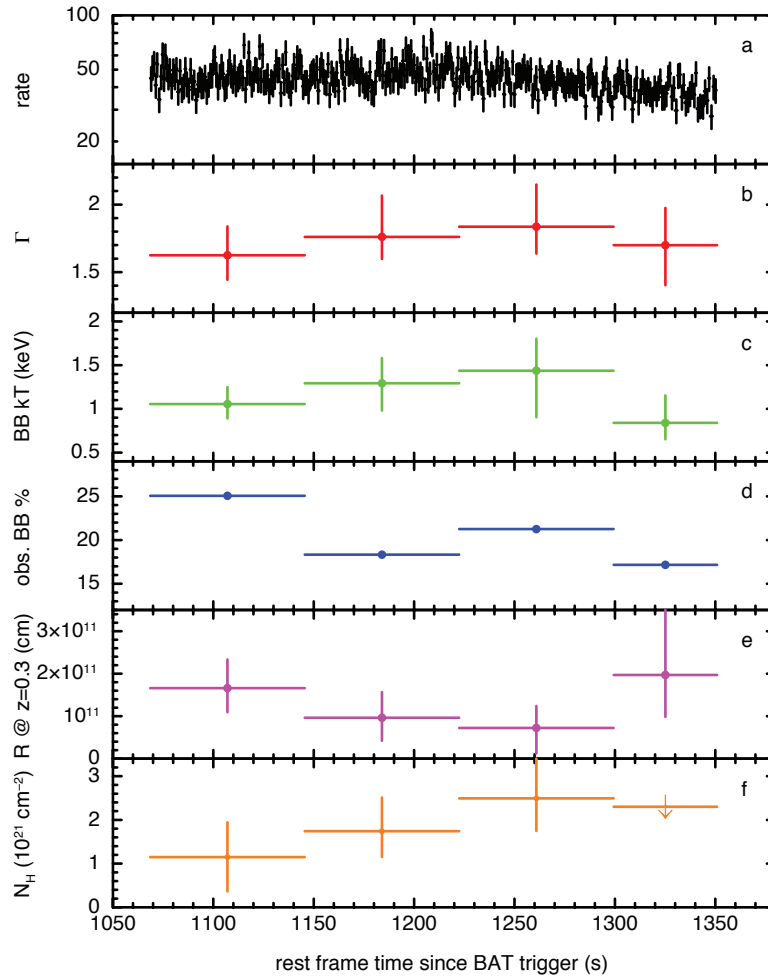
Supplementary Figure 3 | Results from the fits to the first snapshot of the X-ray data. Panels from top to bottom: **a**, count rate during the first snapshot; **b**, photon index Γ; **c**, black body Temperature in keV; **d**, contribution of the black body to the total emission in percent; **e**, radius of the emitting black body at $z = 0.33$; **f**, total absorbing column density in X-rays (the Galactic column density in the line-of-sight is 7.9×10^{20} cm^{-2}).

We also checked for a possible periodicity in the X-ray data. To this end, light curves were extracted with 18 ms bins which is the best time resolution available for WT mode. Using the `Kronos powspec` tool, no significant periodic signal was identified with a frequency between 0.005 and 28 Hz (0.04 and 200 s) in either the first or second snapshot of data. The 3σ limit on the variation in flux of any periodic signal during the first WT snapshot is 6.3%.
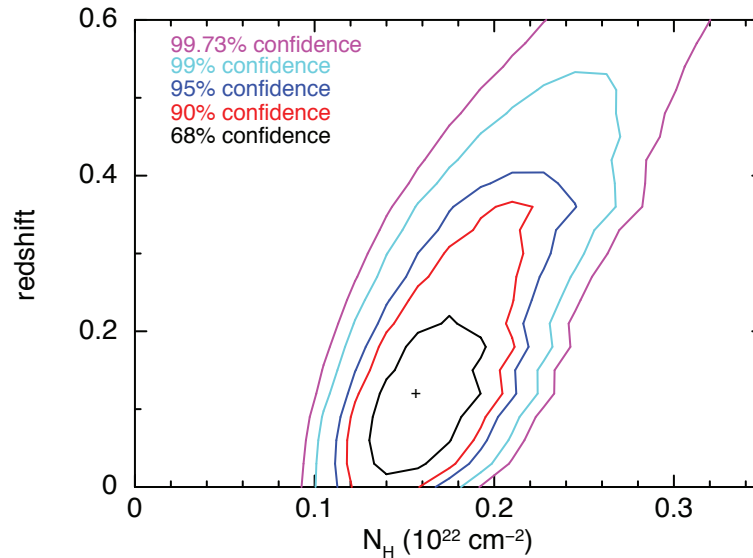
Supplementary Figure 4 | Redshift vs. absorbing column density confidence contours. The fit is based on the data from the first snapshot. Plotted are the 1, 2 and 3 σ contours, 90% and 99% confidence intervals.

3 UV, optical and IR data analysis

3.1 *Swift*/UVOT

Swift/UVOT began observing GRB 101225A 1373 s after the BAT trigger, simultaneous with the XRT observations. The automatic target sequence did not start until the end of the BAT image trigger at ~ 23 minutes. The optical counterpart was found to be blue, with strong detections in the UV filters ($uvw1$, $uvm2$, $uvw2$), weak detections in the b and u filters, and no detection in the v filter. The data were processed using the standard *Swift* software tool `uvotmaghist` within `HEAsoft 6.9` and the latest calibration files (20101231).

We extracted counts using a circular aperture with a radius of 5 arcsec for count rates above 0.5 counts s^{-1}, and a 3 arcsec aperture where the count rate drops below 0.5 counts s^{-1}, as well as a source-free background region. The tool `uvotmaghist` applies coincidence-loss corrections and aperture corrections. The count rates were converted to flux density using standard photometric calibrations [31, 32].

3.2 McD 2.1m

The CQUEAN instrument (Camera for QUasars in the EArly uNiverse; Park et al. 2011, in preparation) on the 2.1m Otto-Struve telescope at McDonald Observatory, Texas, USA, observed the optical counterpart starting at 01:16:23 UT, on Dec. 26, 2010 (6.64 h after the burst). Three exposures of 300 s each were taken in r', i', z', and Y bands under photometric conditions. The data were reduced with standard procedures of dark and flat-field corrections. The afterglow is detected in the r', i', and z'-band images, the Y band gives an upper limit only.

Mid t-t_0 (days)	Exposure (s)	Filter	Telescope	Mag$_{AB}$	Flux (μJy)
Premaging	3×500	g'	3.5mCFHT	>26.9 (27.2±0.5)	<0.06 (0.048±0.22)
Premaging	3×500	i'	3.5mCFHT	>25.5	<0.22
0.01848	168	$w2$	UVOT	>21.36	< 10.38
0.07041	1431	$w2$	UVOT	21.56± 0.20	8.65± 1.80
0.17373	6719	$w2$	UVOT	21.63± 0.11	8.06± 0.88
0.30739	6679	$w2$	UVOT	21.76± 0.12	7.19± 0.85
0.45280	5805	$w2$	UVOT	21.96± 0.15	5.96± 0.91
0.81302	12039	$w2$	UVOT	22.57± 0.17	3.42± 0.58
1.00869	11753	$w2$	UVOT	22.37± 0.16	4.08± 0.67
1.41736	23440	$w2$	UVOT	22.61± 0.20	3.27± 0.66
1.75211	23368	$w2$	UVOT	23.45± 0.30	1.51± 0.49
2.44862	74516	$w2$	UVOT	>23.73	< 1.17
4.07964	138747	$w2$	UVOT	>24.20	< 0.76
7.52954	377712	$w2$	UVOT	>25.39	< 0.25
0.01818	319	$m2$	UVOT	>20.81	< 17.14
0.07515	1431	$m2$	UVOT	21.97± 0.31	5.89± 1.94
0.61452	899	$m2$	UVOT	21.90± 0.21	6.34± 1.33
0.95369	12104	$m2$	UVOT	22.00± 0.15	5.74± 0.83
1.18487	18396	$m2$	UVOT	22.47± 0.23	3.74± 0.87
1.48860	23468	$m2$	UVOT	22.46± 0.19	3.76± 0.73
1.85629	29528	$m2$	UVOT	22.97± 0.22	2.35± 0.53
2.51507	40973	$m2$	UVOT	23.34± 0.30	1.68± 0.53
4.08285	138701	$m2$	UVOT	>24.25	< 0.73
0.01846	318	$w1$	UVOT	>21.15	< 12.64
0.07752	1431	$w1$	UVOT	>22.10	< 5.26
0.65205	5571	$w1$	UVOT	21.81± 0.17	6.88± 1.15
0.96984	16520	$w1$	UVOT	21.72± 0.16	7.46± 1.19
1.37145	18904	$w1$	UVOT	22.23± 0.26	4.65± 1.25
1.71425	29052	$w1$	UVOT	22.46± 0.25	3.76± 0.97
2.44380	74329	$w1$	UVOT	>22.97	< 2.36
4.07673	138760	$w1$	UVOT	>23.22	< 1.86
0.01789	169	u	UVOT	>20.46	< 23.68
0.07228	2579	u	UVOT	21.59± 0.28	8.42± 2.47
1.28374	103571	u	UVOT	22.33± 0.26	4.24± 1.14
2.44533	74215	u	UVOT	>21.82	< 6.80
4.07781	138647	u	UVOT	>22.06	< 5.46
0.01817	169	b	UVOT	>19.94	< 38.37
0.06802	1430	b	UVOT	>20.86	< 16.51
0.16319	6726	b	UVOT	21.53± 0.30	8.83± 2.86
0.30647	8349	b	UVOT	>21.83	< 6.76
1.14624	127458	b	UVOT	>22.19	< 4.85
2.44615	74224	b	UVOT	>21.00	< 14.47
4.07834	138632	b	UVOT	>21.33	< 10.64
0.01789	318	v	UVOT	>19.35	< 66.30
0.07278	1431	v	UVOT	>20.36	< 26.12
0.18317	6538	v	UVOT	>21.04	< 13.96
0.31290	5819	v	UVOT	>20.69	< 19.20
1.11739	21×180	V	1.23mCAHA	22.47±0.19	3.73±0.65
1.18728	121098	v	UVOT	>21.08	< 13.39
2.45087	74279	v	UVOT	>20.50	< 22.93
4.08128	138537	v	UVOT	>20.92	< 15.56
39.11207	6×180	g'	OSIRIS/10.4mGTC	> 26.3	< 0.11
39.49403	5×180	g'	GMOS/8mGemini	26.80±0.35	0.07±0.03
~180	42×200	g'	OSIRIS/10.4mGTC	27.21±0.27	0.047±0.010
1.04545	19×180	R	1.23mCAHA	22.61±0.16	3.28±0.48
0.29887	3×300	r'	CQUEAN/2.1mMcD	22.43±0.14	3.87±0.50
2.08833	1×30	r'	OSIRIS/10.4mGTC	23.39±0.12	1.60±0.18
21.15017	10×60	r'	OSIRIS/10.4mGTC	24.21±0.14	0.75±0.10
28.49818	5×180	r'	GMOS/8mGemini	24.81±0.13	0.43±0.05
39.10159	4×120	r'	OSIRIS/10.4mGTC	24.77±0.13	0.45±0.05
39.47981	5×180	r'	GMOS/8mGemini	25.24±0.15	0.29±0.04
44.08258	4×180	r'	OSIRIS/10.4mGTC	> 24.7	< 0.48
~180	32×200	r'	OSIRIS/10.4mGTC	26.90±0.14	0.063±0.008
1.17359	17×180	I	1.23mCAHA	22.18±0.35	4.88±1.57
61.96267	20×120	I	SCORPIO/6mBTA	25.17±0.35	0.31±0.10
0.29516	3×300	i'	CQUEAN/2.1mMcD	22.72±0.18	2.96±0.49
10.09449	9×900	i'	RAT/2.0mLT	24.01±0.13	0.90±0.11
39.12164	5×60	i'	OSIRIS/10.4mGTC	24.36±0.17	0.65±0.11
39.46336	5×180	i'	GMOS/8mGemini	24.61±0.09	0.52±0.04
0.30384	3×300	z'	CQUEAN/2.1mMcD	22.65±0.34	3.16±1.00
39.09432	6×60	z'	OSIRIS/10.4mGTC	24.73±0.42	0.47±0.18
39.44619	7×180	z'	GMOS/8mGemini	24.77±0.25	0.45±0.10
0.30745	3×300	Y	CQUEAN/2.1mMcD	> 22.5	< 3.63
37.45092	32×60	J	NIRI/8mGemini	> 23.4	< 1.58
28.46873	44×60	K_S	NIRI/8mGemini	24.48±0.35	0.59±0.19

Supplementary Table 2 | Log of UVOIR observations. Values are not corrected for Galactic extinction.

3.3 CAHA 1.23m

The 1.23m telescope is located at the German-Spanish observatory of Calar Alto (CAHA) in Almería, Spain and is equipped with an optical imaging camera. The optical counterpart was detected in the VRI bands $1.04 - 1.11$ days after the GRB trigger. The 1.23m was also used to calibrate the object field in $BVRI$ bands by observing the Landolt fields RU149D and SA98 on Dec. 26 and 27, 2010, under photometric conditions.

3.4 LT 2.0m

The Liverpool telescope is a 2.0m fully robotic telescope located at the observatory of Roque de los Muchachos on La Palma. Observations were carried out with the imaging camera RATCAM. The optical counterpart was detected in one epoch in the i'-band at 10.09 d after the GRB.

3.5 OSIRIS/GTC

We acquired imaging data using OSIRIS at the Gran Telescopio de Canarias (GTC), a 10.4m telescope located at the observatory of Roque de los Muchachos on La Palma, Canary Islands, Spain.

The observations started in r' band $\sim$2 days after the burst, exposing for 30 s. A second r' observation was carried out $\sim$ 21 days after the gamma-ray event, where 5 exposures of 180 s were obtained. We furthermore obtained a late-time SED at 39 days in g', r', i' and z' bands and a last image at $\sim$44 days in the r' band.

The data of our two late epochs (at $\sim$39 and $\sim$44 days) were obtained at a considerable airmass ($1.73 - 2.14$) since the object was setting quickly after evening twilight. The data at $\sim$21 and $\sim$44 days were acquired with the Moon at $\sim$54 and $\sim$36 degrees, respectively, with an illumination of 83% and 21%, respectively. The SED at 39 days was constructed in dark time. The observing conditions were good in all four GTC epochs.

3.6 Gemini-North: NIRI and GMOS-N

Late-time imaging of the optical counterpart of GRB 101225A was conducted with the Gemini-North observatory on Mauna Kea/Big Island, Hawaii, on several occasions. On the night of Jan. 23, 2011 we observed the field with the Near InfraRed Imager (NIRI) in the K' filter for 44×60 s exposures (2×30 s co-adds) before switching to the Gemini Multi-Object Spectrograph (GMOS-N) for 5×180 s exposures each in the r' filter. On the night of Feb. 1, 2011 we re-observed the field with NIRI in the J band for 32×60 s exposures (co-added), and finally on the night of Feb. 3, 2011 we imaged the field in all four GMOS broad-band filters ($g'r'i'z'$). Since the source was setting, all exposures were taken at moderate to high airmass ($1.5 - 2.5$), although under relatively good seeing conditions.

3.7 BTA 6m

A final late image was obtained using SCORPIO on the 6.0m BTA telescope, located at the Special Astrophysical Observatory, in Russia. The observation consisted of 20×120 s exposures using an I filter obtained on Feb. 25, 2011 (60 days post burst) under good weather conditions and a seeing of $1.3 - 2.0$ arcsec.

3.8 Photometry of ground-based data

The photometry of V, R and I data was done in a consistent way using a set of 15 comparison stars in the field of GRB 101225A calibrated with the Landolt fields taken on Dec. 26 and 27, 2011 by the 1.23m CAHA. For r', i' and z' photometric calibrations were done with observations form the 2.1m Otto-Struve telescope at McDonald

Observatory on Dec. 26, 2010, using the standard star Feige 34. Finally, g' photometry was derived from the other reference magnitudes using numerical transformations [33]. The magnitudes of the comparison stars in the different filters used for the optical observations are listed in SI Tab. 3.

We performed aperture photometry using PHOT within IRAF taking an aperture radius equal to the Full Width at Half Maximum (FWHM) of the stellar point sources. In cases where the contamination by neighboring sources was not negligible, we did PSF photometry within IRAF. In SI Tab. 2 we list the final photometry for all UV, optical and IR data.
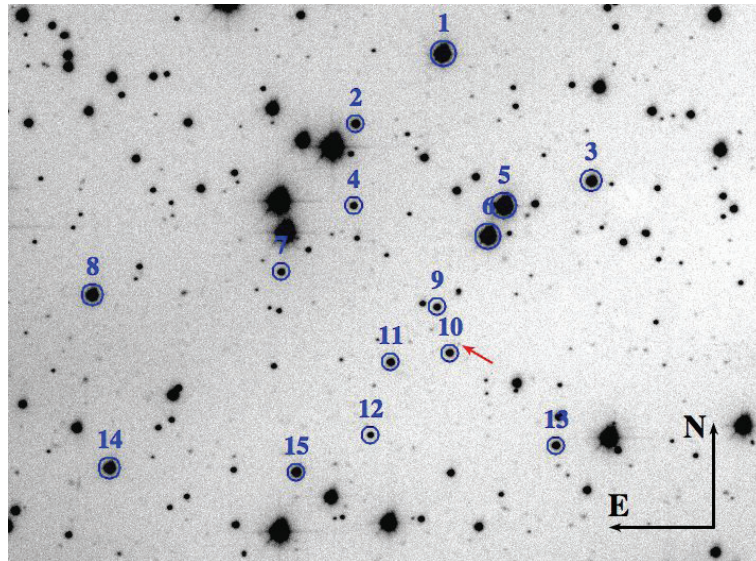
Supplementary Figure 5 | Field with the secondary standards used for the photometric calibration. The position of the optical counterpart of GRB 101225A is indicated with an arrow. The photometric magnitudes of each of the reference stars are given in SI Tab. 3. The field of view is 6 arcmin × 4 arcmin.

ID	RA	DEC	V	R	I	g'	r'	i'	z'
1	00:00:48.13	+44:38:18.9	15.282 ± 0.009	14.916 ± 0.049	14.553 ± 0.052	——	——	——	——
2	00:00:52.02	+44:37:46.6	18.065 ± 0.097	17.268 ± 0.055	16.288 ± 0.110	18.62±0.23	17.679±0.011	17.121±0.010	16.870±0.010
3	00:00:41.58	+44:37:18.0	16.794 ± 0.050	16.421 ± 0.051	15.972 ± 0.062	17.14±0.12	——	——	——
4	00:00:52.13	+44:37:07.9	18.789 ± 0.079	18.335 ± 0.133	18.051 ± 0.162	19.26±0.19	18.464±0.012	18.325±0.011	18.263±0.013
5	00:00:45.46	+44:37:06.6	14.995 ± 0.008	14.633 ± 0.049	14.235 ± 0.051	——	——	——	——
6	00:00:46.18	+44:36:52.4	15.174 ± 0.015	14.838 ± 0.049	14.456 ± 0.051	——	——	——	——
7	00:00:55.37	+44:36:36.8	19.165 ± 0.180	18.268 ± 0.090	17.356 ± 0.188	——	18.569±0.012	17.905±0.011	17.597±0.011
8	00:01:03.76	+44:36:26.8	16.594 ± 0.012	16.161 ± 0.049	15.691 ± 0.090	——	——	——	——
9	00:00:48.48	+44:36:19.3	18.796 ± 0.059	17.924 ± 0.069	16.694 ± 0.092	19.08±0.14	18.602±0.012	17.819±0.011	17.516±0.011
10	00:00:47.98	+44:35:57.8	18.682 ± 0.132	17.901 ± 0.107	17.059 ± 0.182	19.41±0.31	18.174±0.011	17.645±0.010	17.427±0.012
11	00:00:50.58	+44:35:43.5	18.505 ± 0.218	17.877 ± 0.060	17.270 ± 0.163	——	18.088±0.011	17.715±0.010	17.537±0.012
12	00:00:51.59	+44:35:19.1	19.253 ± 0.130	18.893 ± 0.131	18.460 ± 0.273	19.54±0.31	19.059±0.014	18.910±0.013	18.852±0.020
13	00:00:43.29	+44:35:13.1	18.050 ± 0.066	17.749 ± 0.085	17.318 ± 0.108	18.34±0.16	17.853±0.011	17.729±0.010	17.671±0.012
14	00:01:03.09	+44:35:04.8	16.828 ± 0.015	16.321 ± 0.052	15.826 ± 0.087	——	——	——	——
15	00:00:54.83	+44:35:01.9	17.516 ± 0.032	17.024 ± 0.066	16.321 ± 0.082	18.04±0.08	17.148±0.010	16.960±0.010	16.853±0.011

Supplementary Table 3 | Magnitudes of calibration stars used for the optical photometry. A finding chart indicating the position of each reference star is given in SI Fig. 5. Coordinates are in J2000. V, R and I are given in Vega system, the other bands are in AB.

3.9 Preimaging

Preimaging of the field was available from the archive of the 3.5m Canada-France-Hawaii Telescope (CFHT), obtained with the MegaPrime/MegaCam for the Pan-Andromeda Archaeological Survey (PAndAS, [34]). We combined 3×500 s exposures obtained under very good conditions in g' and i' bands and derive 3σ limiting magnitudes for these exposures of $i' > 25.5$ and $g' > 26.9$. At the position of GRB 101225A, we tentatively detect an object with $g' = 27.2 \pm 0.5$ (2σ, see SI Fig. 6) which is consistent with our late host detection (see Sect. 3.10).
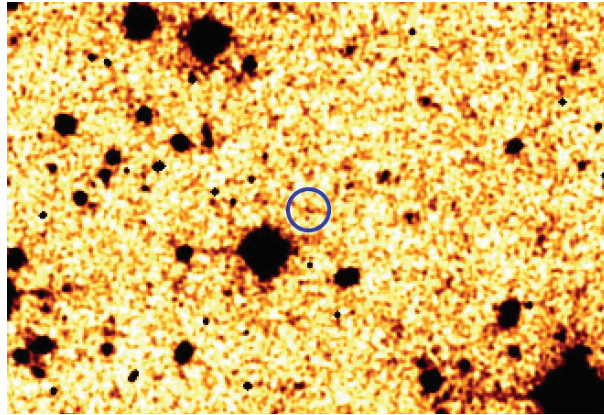
Supplementary Figure 6 | **Pre-imaging exposure in g' band obtained with the 3.5m CFHT.** The circle indicates the position of the optical counterpart of GRB 101225A, with a host galaxy candidate (2σ detection). The field of view is 60 arcsec $\times$ 40 arcsec, North is to the top and East to the left of the image.

3.10 Host detection
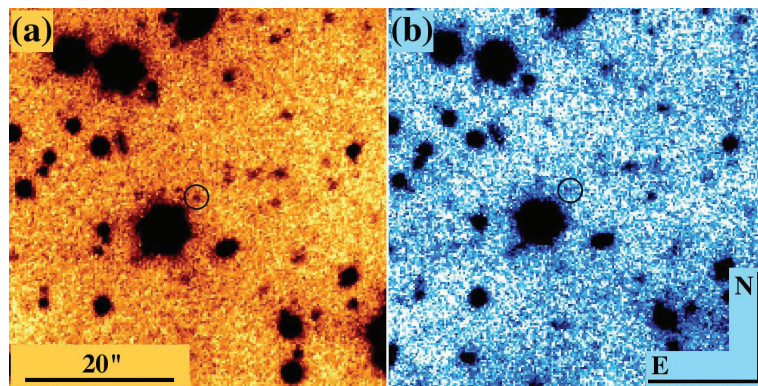
Supplementary Figure 7 | **Imaging of the host using OSIRIS/GTC 6 months after the GRB**. **a**, stacked image in r'; **b**, the same in the g' band. The field of view is 50 arcsec $\times$ 65 arcsec. The circle indicates the position of the host galaxy.

At three epochs, June 9, June 28 and 29, we obtained deep imaging of the field of GRB 101225A in g′ and r′ with OSIRIS at the 10.4m GTC under good conditions and seeing around 1.0 arcsec. The total exposure time is 8400 s in g' and 6400 s in r' band. We detect an unextended object at the position of the GRB in both bands at $g' = 27.21 \pm 0.27$ ($\sim 3\sigma$) and $r' = 26.90 \pm 0.14$ ($\sim 7\sigma$). These values are clearly above the extrapolation of the SN light curve to 180 days and we therefore propose this object to be the host galaxy of GRB 101225A. At a redshift

of $z = 0.33$, the absolute luminosity is $M_{abs,g} = -13.7$ mag, ~ 2 mag fainter than the faintest GRB host detected so far (XRF 060218 [12]) and one of the faintest galaxies ever detected at that redshift. The $g' - r'$ color of the host is consistent with what we would expect for a late-type star-forming galaxy, in line with what is seen for other long GRBs, although we note that the large errors allow other galaxy types as well. The blue color would also argue against the source being a late detection of a cool component from the event itself (see [3]).

4 Optical spectroscopy

We obtained a spectrum of the optical counterpart 51 h after the event using OSIRIS on the 10.4m GTC telescope on La Palma (Spain). Two spectra of 1800 s exposure time each were taken with grism 300B (R=325, wavelength range: $3500 - 7000$ Å) under moderate to high airmass (1.26 and 2.05, respectively). The spectra were reduced and combined with standard tasks in IRAF and flux-calibrated with the spectrophotometric standard G191-2B2 observed in the same night. The continuum is clearly detected, but the spectrum shows no obvious absorption or emission lines.

We performed a search for any possible redshift solution in the range $z = 0.1 - 0.6$. For this, we stacked the normalized spectrum at the position of the strongest emission lines [OII] $\lambda\lambda$ 3727, 3729 Å, [OIII] $\lambda\lambda$ 4959, 5007 Å, Hβ and Hα at redshifts between 0.1 and 0.6 in steps of 0.005. We find no indication of any emission feature in the stacked spectrum at any redshift in this interval.

The limits on the detection of Hα [OIII] and [OII] emission from the host galaxy are $< 5 \times 10^{-18}$ erg cm^{-2} s^{-1}, $< 2.3 \times 10^{-18}$ erg cm^{-2} s^{-1} and $< 3 \times 10^{-18}$ erg cm^{-2} s^{-1} (3σ) respectively. We can also put a limit on the detection of Hα at $z = 0$ of $< 2 \times 10^{-18}$ erg cm^{-2} s^{-1}. The flux-calibrated spectrum with the position of typical emission lines from the host shifted to a redshift of $z = 0.33$ is shown in SI Fig. 8.
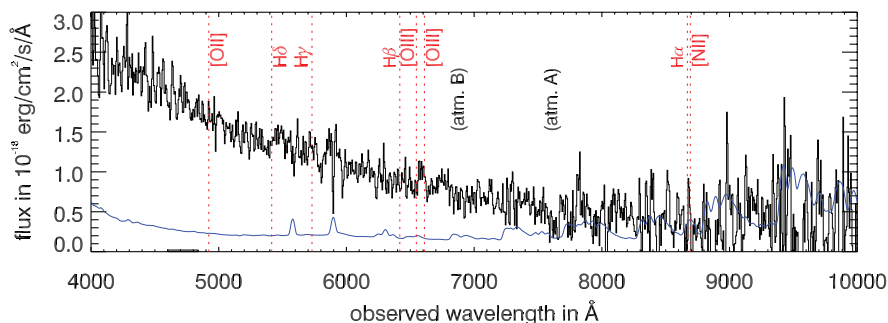
Supplementary Figure 8 | **Flux-calibrated spectrum of the optical transient from GTC/OSIRIS 2.1 days after the GRB**. The error spectrum is plotted in blue. The red lines indicate the position of normally strong emission lines from the interstellar medium at a redshift of $z = 0.33$, none of the lines is detected in our spectrum.

On the night of 2011 Feb. 04 we observed the optical counterpart with the Low-Resolution Imaging Spectrometer [35] on the Keck I telescope during local twilight. Two undithered observations of 600 seconds each were acquired using the 1.0 arcsec slit and the D500 dichroic at a position angle of 86.5 degrees. On the red arm we used the 600/7500 grating and binned the CCD along the spatial direction (2x1 binning); on the blue arm we used the 600/4000 grism and binned the data along both spatial and spectral axes (2x2 binning). Due to twilight there is no evidence of a trace in the blue spectrum (and no source is detected in GMOS g'-band imaging from the previous night). A faint continuum trace at the expected position of the transient is identified on the red side in the second (less twilight-affected) exposure from 7160 to 8000 Å with no absorption or emission features visible.

5 Modeling the UV to NIR spectral energy distribution

The early evolution of the UV/optical/IR (UVOIR) counterpart is very unusual for a GRB afterglow. Instead of a power-law spectrum with a negative spectral slope, it had a very blue counterpart, following what seemed to be a power-law with a positive spectral slope [36]. Furthermore, the counterpart stayed bright during the first days and then decayed [37] with a strong color change, transforming into a very red counterpart two weeks after the trigger [38]. We interpret this early evolution as being produced by the expansion and cooling of a black body, as shown in Section 5.1.

The simple black body evolution is not valid any more for the emission beyond ~ 20 days after the trigger. At that time we observe a flattening of the light curve, while the very red color is preserved. This late evolution can be well-described with the presence of a supernova component, as described in Section 5.2.

5.1 Early time evolution

For the modeling of the UVOIR spectral energy distribution (SED), we use the photometry presented in SI Tab. 2 together with some of the data points extracted from the literature [36, 37, 38, 39, 40, 41, 42]. All magnitudes are corrected for a Galactic extinction of $A_V = 0.33$ mag and transformed from magnitudes to flux densities. With this data set we are able to derive a set of 12 SEDs ranging from 0.07 to 40 days after the trigger.

The early optical SEDs are well fitted by using an expanding and cooling black body of the following form (in frequency space):

$$F_\nu(Jy) = 10^{26} \left(\frac{R}{D}\right)^2 \frac{2\pi h \nu^3 (1+z)^4}{c^2} \frac{1}{e^{h\nu/k_B T_{obs}} - 1} \tag{1}$$

Here, the factor 10^{26} is used to convert $W/m^2/Hz$ to Jy. R is the radius of the emitting black body (which we assume to be spherical), D is the luminosity distance to the object, z the redshift and T_{obs} is the observed black body temperature (the rest-frame temperature would be $T_{rest} = T_{obs}(1+z)$). The other physical constants are: c is the speed of light, h Planck's constant and k_B Boltzmann's constant. For simplicity we assume a black body with an emissivity of 1. The black body succeeds in reproducing the data up to 10 days, without any intrinsic extinction or additional emission component, after which another component becomes dominant (see Section 5.2).

From the fits to the SED evolution and allowing for a second-order fit, we get the following evolution of the normalisation constant:

$$log\left(10^{26}\pi(1+z)^4 \left(\frac{R}{D}\right)^2\right) = (0.70 \pm 0.04) + (0.46 \pm 0.03)log(t) - (0.01 \pm 0.05)log10(t)^2 \tag{2}$$

where t is the time in days. The temperature evolution (in K) can be described by:

$$log\left(T_{obs}\right) = (4.342 \pm 0.017) - (0.395 \pm 0.016)log(t) - (0.11 \pm 0.02)log(t)^2 \tag{3}$$

Figure 9 shows the temporal evolution of the normalisation constant and the temperature. The normalisation can be sufficiently described by a linear evolution in log-log space and therefore the second-order term in eq. (2) can be neglected. For the temperature, we need an additional second-order term to obtain a reasonable fit to the data. The temperature and normalization evolution fits very well to our theoretical model of the afterglow (see Sect. 8 and SI Fig. 19). Once the redshift is known the normalisation constant can be transformed into physical values in the rest-frame of the object which is shown in SI Fig. 10. For this we assume $z = 0.33$ (see Section 5.2), or 1661.1 Mpc using a ΛCDM cosmology with $H_0 = 71$, $\Omega_M = 0.27$ and $\Omega_\Lambda = 0.73$.
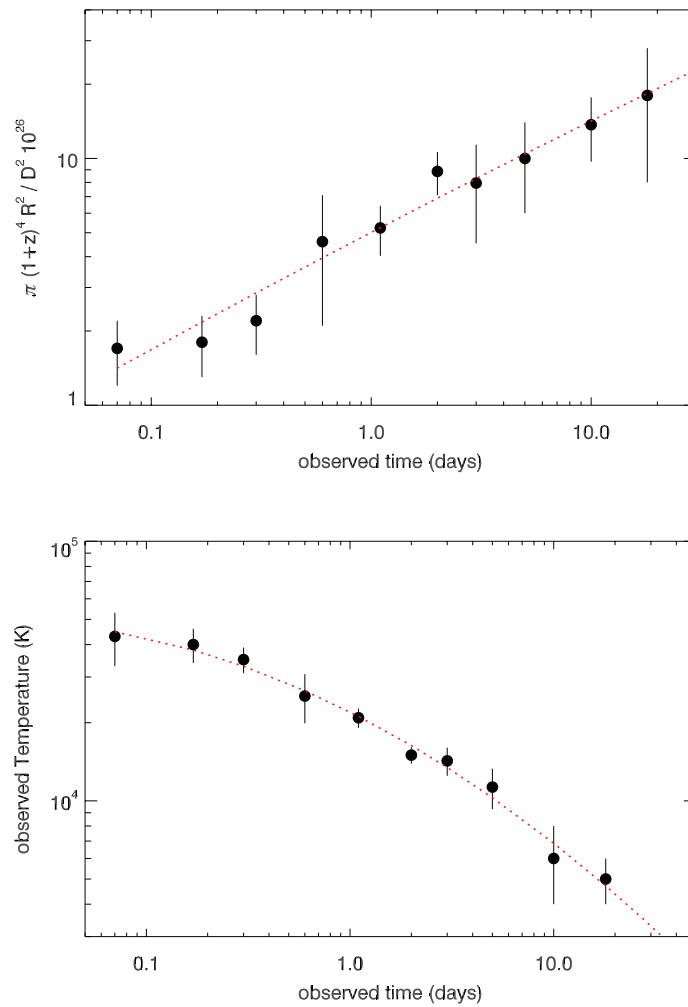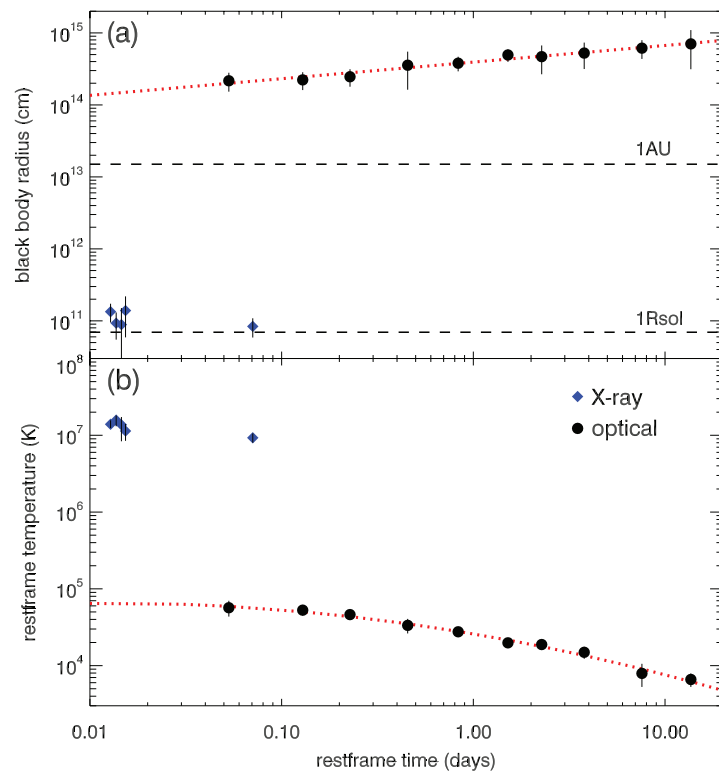
Supplementary Figure 9 | Temporal evolution of the normalization constant (top) and temperature (bottom) during the UVOIR black body phase. The evolution of the normalization constant can be described by a linear evolution in log-log space while the temperature evolution requires a second-order term.

5.2 Late evolution and SN template fitting

The late evolution of the light curve requires a component in addition to the evolving black body described in Section 5.1. A pure black body fit to the late data gives a bad fit with $\chi^2/d.o.f. = 10.45/5$ and is therefore ruled out with a 94% probability. We assume the late SED to have an additional component from a SN and fit the SED with several SN templates. These fits are also used to estimate the redshift of GRB 101225A, which we could not obtain spectroscopically (Section 4).

To determine the redshift of GRB 101225A we use the SED at 40 days after the burst where the contamination from the black body is negligible and where we have detections in 7 different bands. Given the steep slope in the blue part of the spectrum, we convolve the response of each filter with the spectral shape of the templates. This is particularly important for the r'-band observations performed from GTC and Gemini at a very similar epoch, which show a significant difference in flux density. The filter of GTC reaches slightly redder wavelengths, and the

Supplementary Figure 10 | Temporal evolution of the physical radius and temperature of X-ray and UVOIR black body. This figure is identical to SI Fig. 9 but showing the evolution of both black body components together.
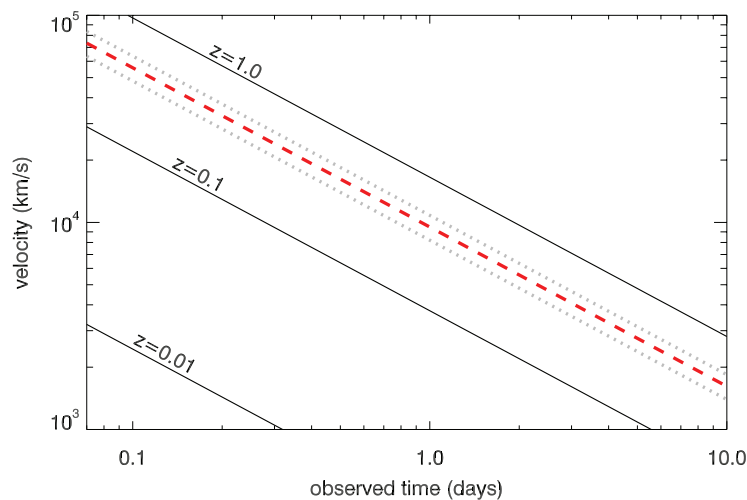
Supplementary Figure 11 | Evolution of the velocity of the UVOIR black body according to the result of our modeling. Red dashed and grey dotted lines: evolution at the best-fit redshift of $z = 0.33^{+0.07}_{-0.04}$, the evolution at $z = 0.01$, $z = 0.1$ and $z = 1.0$ is shown with labeled sold lines. At $z = 0.33$, the velocities derived during the black body phase range between $0.25 - 0.005c$, typical of accelerated material during a supernova explosion.

Epoch (days)	Observed temperature (K)	Normalisation constant $(1+z)^4 \pi 10^{26} \left(\frac{R}{D}\right)^2$
0.07	(43 000±8 000	1.7±1.5)
0.17	40 000±6 000	1.8±1.2
0.3	35 000±3 950	2.2±0.8
0.6	25 340±5 440	4.6±2.5
1.1	20 900±1 770	5.2±1.2
2.0	15 000±1 090	8.9±1.8
3.0	14 260±1 760	8.0±3.4
5.0	(11 300±2 000	10.0±4.0)
10.0	(6 000±2 000	14.0±4.0)
18.0	(5 000±1 000	18.0±10.0)

Supplementary Table 4 | Measured values for the black body evolution. Values in brackets are extrapolated from the black body evolution due to a limited amount of data points in those SEDs.

difference in flux densities can be well explained by a very steep slope due to a SN feature as shown in SI Fig. 12.

We obtain templates for different core-collapse supernovae from the literature [1]. We exclude a SN Ia template from the analysis, as we do not expect high-energy emission such as detected for GRB 101225A for those events. The template for each SN prototype was interpolated to the time of the SED for a range of redshifts (see references in SI Tab. 5). In the particular case of SN 1998S the templates were created by combining ground-based and HST spectra.

In order to obtain the best-fit redshift, we also need to consider the time evolution and maximum of the SN light curve which is expressed as the stretching factor (a stretching factor of $s = 1$ corresponds to a time evolution identical to the corresponding template SN). To this end, we iteratively fit the SED and the light curve starting with $s = 1$ and a first fit to the SED in 7 bands (see SI Fig. 12). With the best-fit z, a SN light curve is derived and fitted to the real light curve which gives a new stretching factor. This process continues until the solutions for s and z converge. We also allow for a scaling of the flux of the SN during the fit. The best fits for s and z for each SN template are displayed in SI Tab. 5.

SN Type	SN template	best fit z	stretching factor	$\chi^2/d.o.f.$	rejection prob.	reference
Ib/c	1999ex	$0.31^{+0.05}_{-0.10}$	1.1±0.15	5.80/5	67%	[43]
Ic broad-lined	**1998bw**	$\mathbf{0.33^{+0.07}_{-0.04}}$	**1.25±0.15**	**3.60/5**	**39%**	**[44, 45]**
II	1998S	$0.50^{+0.07}_{-0.08}$	1.0 ±0.15	44.5/5	100%	[46, 47, 48]
IIN	2001aj	—	—	> 50.0/5	100%	[49]
IIL	1985P	$0.43^{+0.04}_{-0.05}$	1.3 ±0.15	6.1/5	70%	[50]
IIP	1999em	$0.41^{+0.05}_{-0.03}$	1.0 ±0.15	6.3/5	72%	[51]

Supplementary Table 5 | Fits of the SED with SN templates. A pure black body fit (not listed in this table) is rejected with a probability of 94%.

The absolute best fit is obtained with a SN 1998bw template, a broad-lined Type Ic that is the canonical template for GRB-related supernovae. For this case we obtain a redshift of $z = 0.33^{+0.07}_{-0.04}$ and $s = 1.25 \pm 0.15$. The other core-collapse SNe we tested (excluding the Type II SN 1998S, which clearly does not fit our SED) give redshifts between $z = 0.31$ and $z = 0.50$. We therefore use $z = 0.33$ as reference in this work. Figure 12 shows the fitted

---

[1]http://supernova.lbl.gov/~nugent/nugent_templates.html

SED with the template at $z = 0.33^{+0.07}_{-0.04}$ and Figure 13 the best fits for all other SN templates as well as a simple black body.
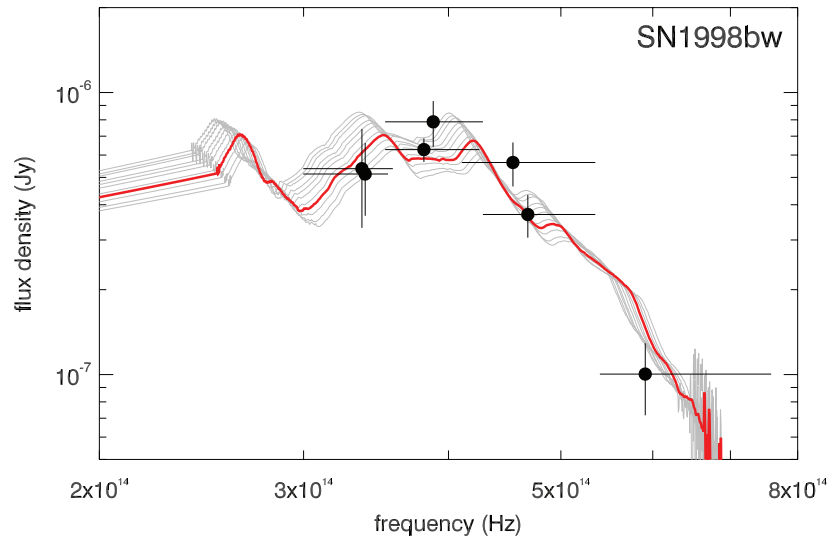
Supplementary Figure 12 │ **Fit of the day 40 SED to a SN 1998bw template.** Observed photometric points in black, the red solid line shows the best fit with $z = 0.33$. Gray lines represent the template at the different redshifts (steps of 0.01) within the errors (+0.07/–0.04).
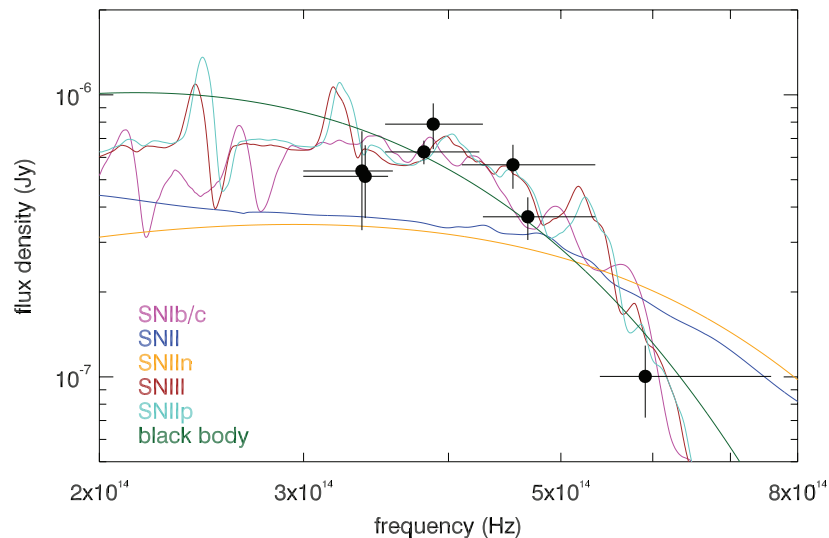
Supplementary Figure 13 │ **Fit of the SED at 40 days to SN templates other than a SN 1998bw-like** (as listed in SI Tab. 5) The fit shown (color code see key) is the one with the best-fit stretching factor for each template. We also plot a simple black body with 3650 K, the temperature at which we obtain the best fit.

5.3 Luminosity and stretching factor of the SN associated with GRB 101225A in the context of other GRB-SNe

We undertake a more general comparison to SNe associated with GRBs by following the formalism of [52]. These authors used a SN 1998bw template light curve to fit late bumps in GRB afterglow light curves, modifying the template by increasing or decreasing the luminosity at peak (the parameter k, with $k = 1$ implying a peak luminosity identical to that of SN 1998bw), and stretching or compressing the light curve in time while retaining the overall shape (the parameter s, again, $s = 1$ implies the temporal evolution is identical to that of SN 1998bw in the same band). This procedure also included the creation of synthetic templates by interpolating between the SN 1998bw light curve in different filters, and taking into account the cosmological K-correction. Nearly all GRB-SNe were well-fit by the SN 1998bw light curve template. For GRB 101225A we have $s = 1.25 \pm 0.15$ and $k = 0.08 \pm 0.03$ according to the designation of [52] using the SN 1998bw light curve at $z = 0.33$.

Ferrero et al. [53] analyzed SN 2006aj associated with XRF 060218, and placed it into the $k - s$ context. They employed the line-of-sight extinction values derived by [54] to derive intrinsic k values. To place the SN associated with GRB 101225A into the $k - s$ context, we fit the light curve analogous to [52], and use the sample of [53] as well as additional events as a comparison. The complete data are presented in SI Tab. 6.

GRB 990712 has been analysed again with additional data. We find no evidence for host extinction. For GRB 021211, a re-analysis of the afterglow SED finds no evidence for host extinction, the value from [53] thus remains unchanged but now counts as extinction-corrected. For GRB 040924, we use the k and s values from [9] and correct k with the extinction found by [54]. For GRB 050525A, we use the uncorrected k value from [53], and correct it with the extinction found by [11]. For XRF 050824, we use the uncorrected k value from [55], and correct it with the extinction found by [11]. GRB 060729 is analysed in [56]. GRB 080319B is analysed in [57]. GRB 090618 has been analysed for this work, using the data set of [18]. We were not able to derive a good SED for this afterglow, therefore the k value has not been corrected.

As can be seen in SI Fig. 14, the SN associated with GRB 101225A is significantly fainter than any other known GRB SN (with the SN associated with GRB 040924 being the most similar, but this event is only marginally detected). At the same time its temporal evolution is similar but slightly slower than most known GRB-SNe, though not by a large amount. It is also fainter than two well-studied Type Ic SNe, SN 1994I and SN 2002ap (see [53] for discussion), the latter being broad-lined, but not associated with a GRB.

6 Discussion on the redshift of GRB 101225A

Determining the distance scale at which GRB 101225A occurred is crucial to understand the energetics and get a clear picture of the physics involved in this event. In this section, we present several independent arguments to strengthen our redshift estimation.

The first strong limit on the redshift comes from the UVOT detection in $uvw2$ which implies a redshift lower than $z = 1.4$ [58]. As an independent test, the analysis of the absorption in the X-ray spectra (see Sect. 2 and in particular SI Fig. 4) imposes an upper limit on the redshift of 0.5 within 99% confidence and 0.35 within 90% confidence.

The most restrictive redshift estimate comes from the SN fitting at 40 days after the burst (see Sect. 5.2), where we find a best fit for a broad-lined SN Ic, such as SN 1998bw, the prototype of GRB-related SNe, at $z = 0.33^{+0.07}_{-0.04}$. For the rest of the SN types that give a reasonable fit, we obtain similar values, always resulting in a redshift between 0.21 and 0.50. Independently of the SN fit, we can compare the brightness of the bump in the light curve with the
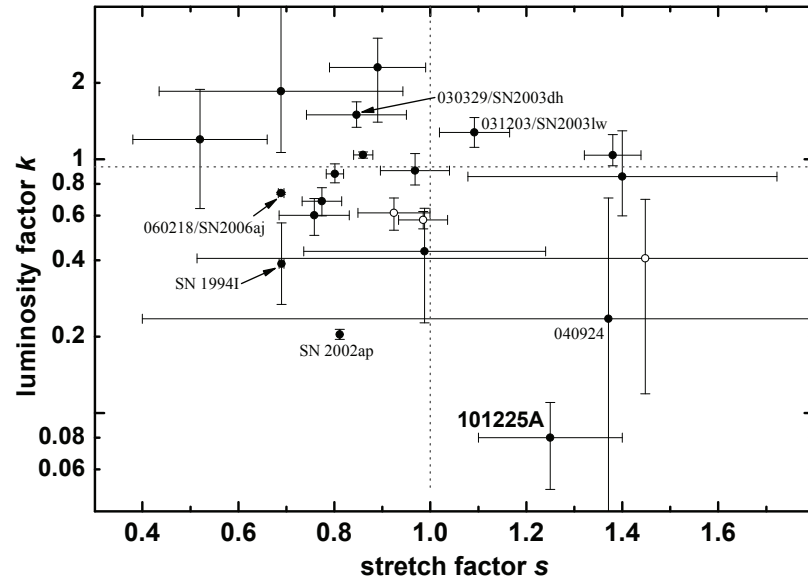
Supplementary Figure 14 | Luminosity factor k **and stretching factor** s **of SNe associated with GRBs.** Filled symbols have been corrected for host-galaxy line-of-sight extinction, non-filled symbols have not. We label several well-studied nearby GRB-SNe, as well as two "canonical" Type Ic SNe, SN 1994I (Ic) and SN 2002ap (broad-lined Ic unassociated with a GRB). The GRB 101225A SN is fainter than all these events.

GRB	k	s	Comment	Reference
970228	0.41 ± 0.29	1.45 ± 0.93	uncorrected	[53]
990712	0.60 ± 0.10	0.76 ± 0.07		This Work
000911	$0.85^{+0.44}_{-0.26}$	1.40 ± 0.32		[53]
010921	$1.85^{+2.82}_{-0.79}$	0.69 ± 0.25		[53]
011121	$0.88^{+0.08}_{-0.07}$	0.80 ± 0.02		[53]
020405	$0.90^{+0.15}_{-0.11}$	0.97 ± 0.07		[53]
020903	0.62 ± 0.09	0.92 ± 0.08	uncorrected	[53]
021211	0.43 ± 0.21	0.99 ± 0.25		[53] , This Work
030329	$1.50^{+0.19}_{-0.16}$	0.85 ± 0.10		[53]
031203	$1.28^{+0.18}_{-0.16}$	1.09 ± 0.07		[53]
040924	$0.24^{+0.47}_{-0.23}$	1.37 ± 0.97		[10], [54]
041006	$1.04^{+0.22}_{-0.09}$	1.38 ± 0.06		[53]
050525A	$0.68^{+0.09}_{-0.08}$	0.77 ± 0.04		[53] , [11]
050824	$1.20^{+0.69}_{-0.56}$	0.52 ± 0.14		[55] , [11]
060218	0.74 ± 0.01	0.69 ± 0.01		[53]
060729	1.04 ± 0.03	0.86 ± 0.02		[56]
080319B	$2.30^{+0.70}_{-0.90}$	0.89 ± 0.10		[57]
090618	0.58 ± 0.05	0.99 ± 0.05	uncorrected	This Work, [19]
101225A	0.08 ± 0.03	1.25 ± 0.15		This Work

Supplementary Table 6 | Luminosity Factor k **and Stretching Factor** s **for GRB SNe**

dimmest known SN (SN2008ha, which peaked at $M_R = -14.5 \pm 0.3$, [59]) and take that as a lower limit on the redshift. In this case, we would expect GRB 101225A to be located at a redshift larger than 0.1.

From the SED fit of the first days, we know that the evolution is well-described by a simple black body. Depending on the distance at which the object is found, we can derive different radii and expansion velocities. For an explosion of this type, we expect expansion velocities larger than $\sim 10^3$ km s^{-1}, which would be at the edge

of a stellar wind regime and, if similar to a SN explosion, of the order of 10^4 km s^{-1}. We cannot, in principle, rule out higher velocities of the ejecta. Under the assumption that the ejecta should not be traveling at velocities larger than 100,000 km s^{-1} ($0.3c$) and lower than 1,000 km s^{-1} ($0.03c$), we can estimate a range of reasonable velocities between $z \sim 0.20$ and $z \sim 0.60$ (see SI Fig. 11). We note that there might be additional effects such as variations in the transparency of the black body that could modify the results of this simplified analysis. In any case, the evolution of the black body is difficult to reconcile by any source within the Local Group. At a redshift of $z = 0.33$, the velocity of the black body would have evolved from $\sim 70,000$ km s^{-1} at the time of our first SED to $\sim 2,000$ km s^{-1} at the time of our last black body dominated epoch, nicely matching the requirements. The fact that the black body detected for XRF 060218/SN 2006aj was very similar to the one found for GRB 101225A when placed at a redshift of $z = 0.33$ (see Section 7) adds additional evidence for the validity of the redshift estimate.

Concluding, the proposed redshift for GRB 101225A of $z = 0.33^{+0.07}_{-0.04}$ is supported by several independent arguments, and can be considered as a firm reference when studying the physical processes involved in the event. We do not find any evidence that would indicate a redshift smaller than $z = 0.2$ or higher than $z = 0.5$.

7 Comparison between GRB 101225A and other GRBs with SNe and black body components

In SI Tab. 7, we compare several properties of GRBs associated with SNe and without a "classical" afterglow component. All of them are subluminous compared to the average long-duration GRB with E_{iso} around $10^{51} - 10^{54}$ erg. GRB 101225A lies on the lower end of the energy output for normal long-duration GRBs. Among those nearby GRB-SNe without a classical afterglow, there is a class of very long duration GRBs with very low E_{peak} values, all of them showing a thermal component in X-rays. XRF 060218 and XRO 080109 also had a thermal component at optical wavelengths during the first few days [13, 22]. For XRF 100316D, no optical counterpart was detected before the onset of the actual SN due to high intrinsic extinction in the host galaxy.

GRB	z	TC?	T_{90} (s)	E_{peak} (keV)	E_{iso} (erg)	HR(50-100)	Radio?	SN M_V (mag)	Host M_B
980425	0.0085	No	23.3	55±21	8.1×10^{47}	—	Yes	−19.42	−17.6
031203	0.105	No	30	158±51	3×10^{49}	—	Yes	−20.39	−21.0
060218	0.0331	Yes	∼2100	4.9	6.2×10^{49}	0.835	Yes	−18.76	−15.9
080109*	0.0065	Yes	∼400	low	2×10^{46}	—	Yes	−16.7	−20.7
100316D	0.059	Yes	>1300	—	3.1×10^{49}	0.891	No	−18.62	−18.8
101225A	0.33	Yes	>2000	38±20	$> 1.4 \times 10^{51}$	1.06	No	−16.9	−13.7

Supplementary Table 7 | GRBs with SNe but without afterglows * means that no γ-rays were observed, numbers listed are derived from X-rays. TC? refers to the early thermal component, mostly attributed to a supernova breakout. HR is the hardness ratio, defined as the ratio of channels $(50 - 100 \text{ keV})/(25 - 50 \text{ keV})$. SN M_V is the SN peak absolute magnitude in V. Host M_B is the host absolute magnitude in B

XRF 060218 [13] shows a similar early behavior to GRB 101225A. We compare the early UVOT light curve of XRF 060218, which we obtained from the UVOT catalogue [60], to the light curve from GRB 101225A by shifting that of XRF 060218 to $z = 0.33$, including a K-correction. To obtain the K-correction, we use XSPEC assuming a black body spectrum with kT ~ 3.7 eV. The temperature was determined from the best-fit model of a black body to a SED of XRF 060218 taken at 120 ks after the trigger [13]. Using this black body spectrum, we determined the expected flux density in the observed frame for each filter and at $z = 0.33$. The ratio of these two flux densities was
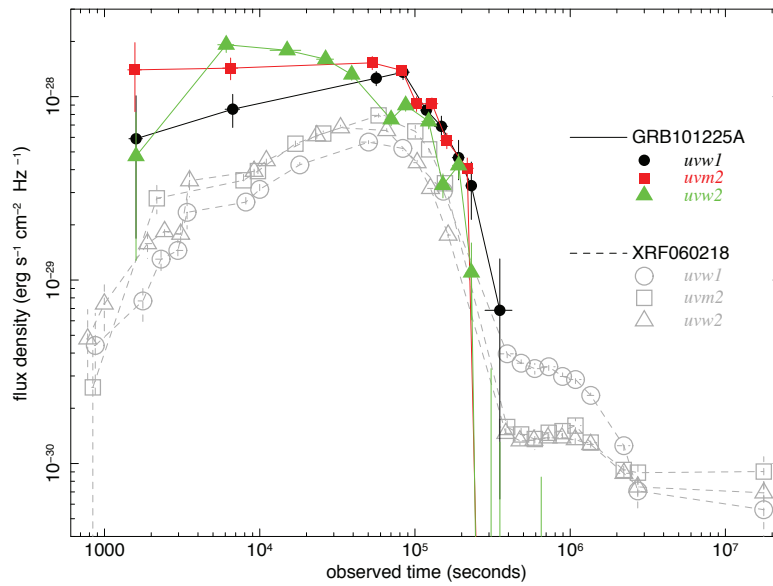
Supplementary Figure 15 | UV light curves in flux density for GRB 101225A and XRF 060218. The light curves for XRF 060218 have been shifted to $z = 0.33$ for direct comparison. The colored solid shapes connected by solid lines are for GRB 101225A, open symbols and dotted lines for XRF 060218. Circles are $uvw1$, squares are $uvm2$, triangles are $uvw2$.

taken to be the K-correction for the specific filter, which is ~ 2.20 for all filters. Figure 15 compares the flux-density light curves of the 3 UV filters of both GRBs. For both GRBs the light curves were corrected for Galactic extinction.

We furthermore performed a fit of the early UVOIR SEDs of XRF 060218 and SN 2008D, in a similar way to what we did for GRB 101225A. XRF 060218 also seems to follow a black body evolution at early times. However, the SN starts to dominate already around 3 days after the burst (see SI Fig. 16), limiting how long the study of the evolution is possible. As can be seen from SI Fig. 17, the evolution of the black body is not very different from what we see in GRB 101225A, although the radius expansion is slightly steeper. SN 2008D does not have a measurable thermal component in the early X-ray data. In the optical, the cooling black body dominates until about 4 days after the event when the onset of the SN was observed (see SI Fig. 16). The temperature of the UVOIR black body of SN 2008D is lower ($\sim 30\,000$ K) than those of XRF 060218 and GRB 101225A. The radius evolution is considerably steeper than for those two events (SI Fig. 17). The UVOIR black body emission of SN 2008D is therefore likely due to the cooling of the initial shock breakout.

8 Temperature evolution and geometry of the UVOIR black body

The interaction of an ultra-relativistic, well-collimated jet (having a half-opening angle $\theta_{j,0} \sim 10°$) with the previously ejected broad torus can explain the power-law and thermal component in the X-rays of GRB 101225A. In SI Fig. 18 we show four different stages in the evolution of the jet and its interaction with the CE shell.

Taking the results from CE-simulations, we assume that the density of the common envelope ejecta in a narrow funnel around the symmetry axis of the system is much lower than elsewhere in the CE-ejecta. This funnel has an opening half-angle $\theta_f \sim 2°$, which permits the passage of the γ-radiation generated by internal shocks in the ultra-relativistic jet. Since $\theta_f < \theta_{j,0}$, most of the jet beam hits the inner boundary of the CE-ejecta at a distance of
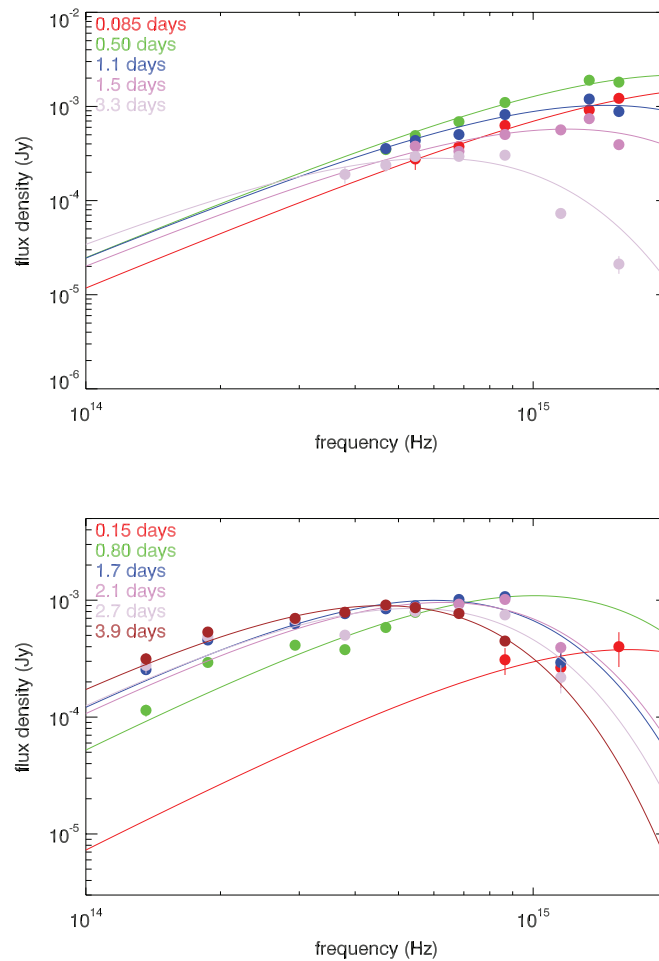
Supplementary Figure 16 | SED fit of the early UVOIR data of XRF 060218/SN 2006aj (top) and SN 2008D (bottom).
The last epoch in both plots already begin to show a strong contribution of the SN. These figures can be directly compared
to Fig. 1 of the main paper.

$R_{CE,in} \simeq 2.5 \times 10^{12}$ cm (panel a of SI Fig. 18), while only a small fraction of the beam propagates through the
funnel until it reaches the outer radial boundary of the CE-ejecta ($R_{CE,out} \simeq 2.1 \times 10^{14}$ cm, panel b). As the central
jet spine progresses through the ejecta funnel, it interacts with the lateral walls, giving rise to mass entrainment in
the jet. The additional baryon load and the shear with the funnel walls decelerates the ultra-relativistic jet spine
extremely quickly and, therefore, no regular afterglow signature is produced. Furthermore, most of the jet beam hits
regions of the CE-ejecta which are much denser than the central funnel and, thus, its propagation across the ejecta
is much slower than that of the central spine. As the jet decelerates to moderately relativistic speeds it expands
laterally.

The X-ray emission is attributed to the shocks (forward and reverse) produced as the ultra-relativistic jet im-
pinges against the inner radial boundary of the CE-ejecta. In our model the cross-sectional radius of the CE-ejecta
funnel ($R_f = R_{CE,in} \sin \theta_f \sim 10^{11}$ cm) sets the almost-constant size of the observed X-ray source (blue dots in SI
Fig. 10).

An approximate evolution of the jet spine as it crosses the ejecta funnel can be obtained by applying the model
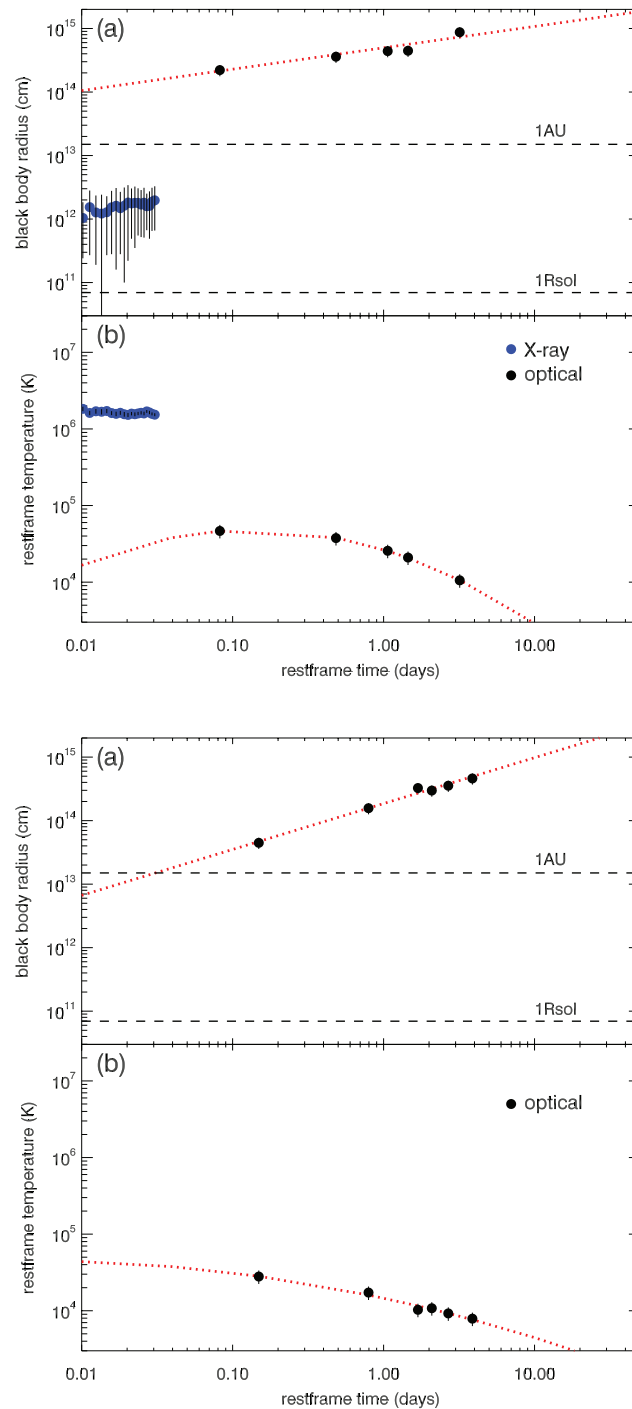
Supplementary Figure 17 | Temporal evolution of the radius and temperature for the pre-SN epochs of XRF 060218/SN 2006aj (top) and SN 2008D (bottom). The dotted line shows a polynomial fit to the temperature and radius evolution. This figure can be directly compared to SI Fig. 10.

of [63], which is based on solving a system of four ordinary differential equations (as a function of the observer's time t) for the Lorentz factor, the rest-mass, the radius and the jet half-opening angle, respectively:
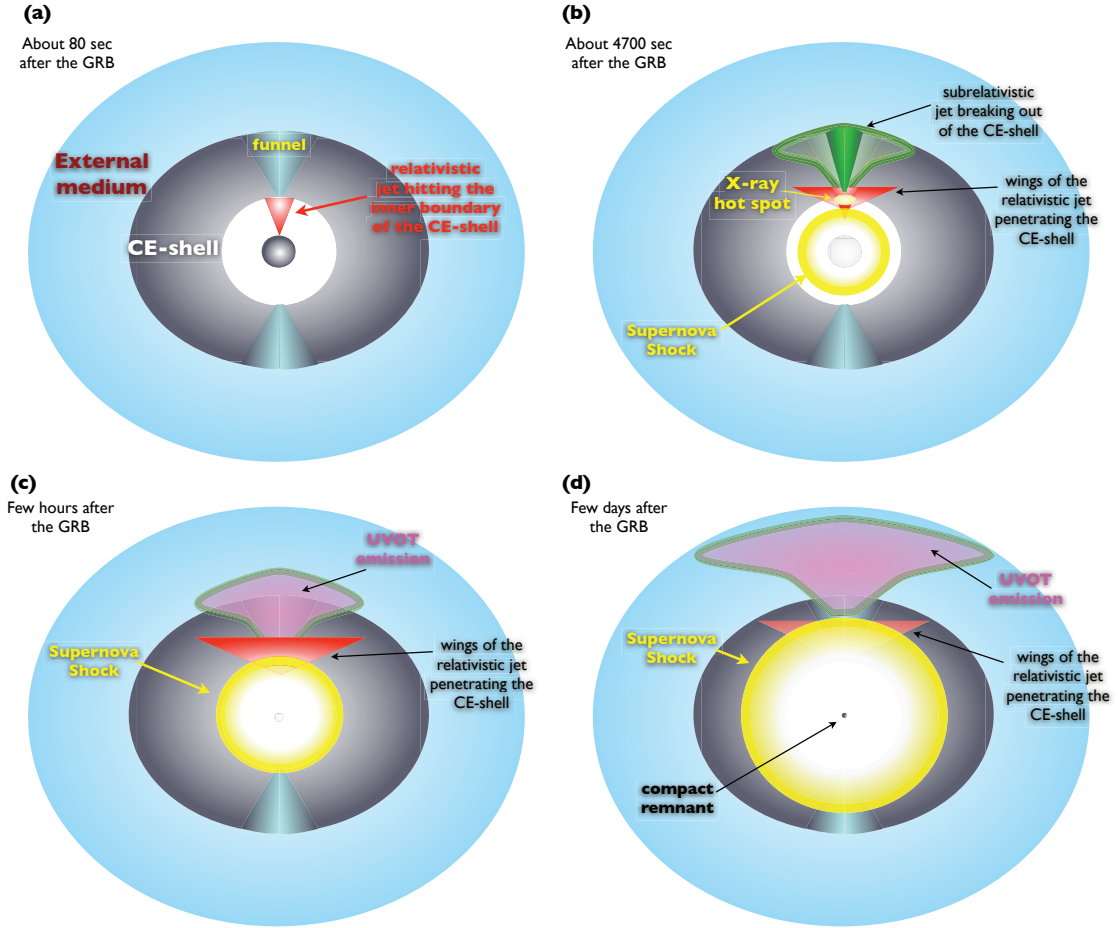
Supplementary Figure 18 | **Cartoon of the different stages in our model of GRB 101225A.** The different stages are explained in the text.

$$\frac{d\Gamma}{dt} = \frac{dm}{dt}\frac{1-\Gamma^2}{M_{jet}+\epsilon m+2(1-\epsilon)\Gamma m} \tag{4}$$

$$\frac{dm}{dt} = \frac{dR}{dt}2\pi R^2(1-\cos\theta)n(R) \tag{5}$$

$$\frac{dR}{dt} = \beta c\Gamma(\Gamma+\sqrt{\Gamma^2-1}) \tag{6}$$

$$\frac{d\theta}{dt} = \frac{c_s(\Gamma+\sqrt{\Gamma^2-1})}{R}, \tag{7}$$

where $n(R)$ is the particle number density, $\beta=\sqrt{1-\Gamma^{-2}}$ is the velocity, ϵ is the shock-generated thermal energy (in the comoving frame) that is radiated, and $c_s=\sqrt{(4\Gamma+1)(\Gamma^2-1)(3\Gamma(4\Gamma^2-1))^{-1}}$ is the sound speed. The temperature of the jet spine is derived by assuming that the pressure is dominated by the photon radiation, so that $P(t)=aT^4(t)/3$, with the radiation constant $a=7.56\times10^{-15}\,\mathrm{erg\,cm^{-3}K^{-4}}$, and noting that $P=(\Gamma^2-1)/(3\Gamma)nm_pc^2$, ($m_p$ being the proton mass) according to [63].

For the jet spine propagating through the CE-ejecta funnel we may take the following initial conditions, corresponding to an ultra-relativistic and cold jet: $\Gamma_{in}\sim100$, $M_{in}\simeq8\times10^{-9}M_\odot$, $R_{in}=R_{CE,in}=2.5\times10^{12}$ cm,

and $\theta_{in} = \theta_f = 2°$. A moderate radiative efficiency $\epsilon \simeq 0.4$ is assumed. The initial jet mass is estimated from the observed lower limit of $E_{\gamma,iso}$ and the initial jet half-opening angle as $M_{jet} = E_{jet}/(((\Gamma - 1)(1 - \epsilon) + \epsilon)c^2)$, where $E_{jet} = E_{\gamma,iso}(1 - \cos\theta_f) \simeq 8.5 \times 10^{47}$ erg. We assume that the CE-ejecta have a declining particle number density of the form $n(R) = n_{in}(R_{CE,in}/R)^2$, with $n_{in} = 4.9 \times 10^{12}$ cm^{-3}. After $t \simeq 0.05$ days the jet spine reaches $R_{CE,out}$ at a velocity of $v_{jet,out} \sim 0.25c$, an opening half-angle of $\theta_{jet,out} \simeq 70°$, and having plowed $\simeq 1.5 \times 10^{-5} M_\odot$ of the CE-ejecta.

The temperature and radius evolution of the UVOIR black body (panel c in SI Fig. 18) can be modeled as the result of the further deceleration of the sub-relativistic jet emerging through $R_{CE,out}$. Again, we use equations 4–7, but now considering a uniform medium with a particle density of $n_{ext} \simeq 1.6 \times 10^9$ cm^{-3} and a higher radiative efficiency of $\epsilon = 1$. As initial conditions we take the terminal values of the velocity, mass, radius and opening half-angle of the previous evolution through the CE-ejecta funnel. The result can be seen in SI Fig. 19 (after $t \simeq 0.05$ days). Small variations of the initial variables can also roughly fit both the radius and the temperature evolution. We note that, even though the theoretical model does not predict an exact power-law for the radius evolution, the deviations from the observed $R(t) \propto t^{0.22}$ are rather small. We also point out that the temperature evolution is not compatible with a single power-law as the observational data suggests.

Finally, we speculate on the fate of the jet wings, i.e., the fraction of the jet that does not cross the CE-ejecta funnel. The energy contained in these wings, $\sim 10^{49}$ erg, is transferred to the CE-ejecta, and can break out through $R_{CE,out}$ on scales of $\sim$ few days, almost isotropically, but at relatively low temperatures compared with the emerging jet spine. Hence, its observational signature will be probably hidden by the emerging SN light curve (panel d in SI Fig. 18).
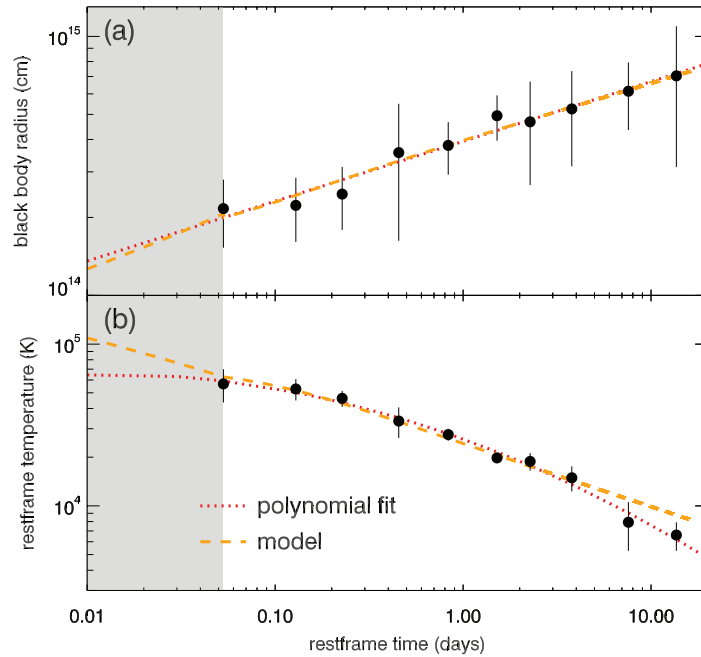
Supplementary Figure 19 | Radius (a) and temperature (b) evolution of a sub-relativistic jet. The initial evolution up to $\simeq 0.05$ days (grey shaded area), is computed with a modified version of the [63] method to incorporate a shell profile in which the number density decays with radius as $n = n_{in}(R_{CE,in}/R)^2$, with $n_{in} = 4.9 \times 10^{12}$ cm^{-3}. For this part of the evolution, the initial data are: $R_{in} = R_{CE,in} = 2.5 \times 10^{12}$ cm, $E_{jet} \simeq 8.5 \times 10^{47}$ erg, $\Gamma_{in} \sim 100$, $\theta_{in} = \theta_f = 2°$, and $\epsilon \simeq 0.4$.

References

[23] Gehrels, N. *et al.* The Swift Gamma-Ray Burst Mission. *Astrophys. J.*, **611**, 1005-1020 (2004)

[24] Racusin, J. L. *et al.* Trigger 441015: Swift detection of a possible burst or transient. *GCN Circ.* **11493** (2010)

[25] Palmer, D. M. *et al.* GRB 101225A, Swift-BAT refined analysis. *GCN Circ.* **11500** (2010)

[26] Cummings, J. R., & Sakamoto, T. GRB 101225A Late-time emission observed by Swift-BAT. *GCN Circ.* **11504** (2010)

[27] Holland, S. T. *et al.* GRB 090417B and its host galaxy: A step toward an understanding of optically dark gamma-ray bursts. *Astrophys. J.*, **717**, 223-234 (2010)

[28] Serino, M. *et al.* GRB 101225A: MAXI/GSC observations. *GCN Circ.* **11505** (2010)

[29] Wilms, J., Allen, A., & McCray, R. On the absorption of X-rays in the interstellar medium. *Astrophys. J.*, **542**, 914-924 (2000)

[30] Verner, D. A. *et al.* Atomic data for astrophysics. II. New analytic FITS for photoionization cross sections of atoms and ions. *Astrophys. J.*, **465**, 487-498 (1996)

[31] Poole, T. S. *et al.* Photometric calibration of the Swift ultraviolet/optical telescope. *Mon. Not. R. Astron. Soc.*, **383**, 627-645 (2008)

[32] Breeveld, A. A. *et al.* Further calibration of the Swift ultraviolet/optical telescope. *Mon. Not. R. Astron. Soc.*, **406**, 1687-1700 (2010)

[33] Jester, S. *et al.* The Sloan Digital Sky Survey view of the Palomar-Green bright quasar survey. *Astron. J.*, **130**, 873-895 (2005)

[34] Richardson, J. C. *et al.* PAndAS' progeny: extending the M31 dwarf galaxy cabal. *Astrophys. J.* **732**, 76 (14pp) (2011)

[35] Oke, J. B. *et al.* The Keck low-resolution imaging spectrometer. *Pub. Astron. Soc. Pac.*, **107**, 375-385 (1995)

[36] Cenko, S. B. GRB 101225A: P60 Observations. *GCN Circ.* **11506** (2010)

[37] Xu, D., Hakala, P., & Fynbo, J. P. U. GRB 101225A: optical break from NOT observation. *GCN Circ.* **11508** (2010)

[38] Tanvir, N. R. *et al.* GRB 101225A: HST observations – no host detected. *GCN Circ.* **11564** (2011)

[39] Xu, D., Ilyin, I., & Fynbo, J. P. U. Trigger 441015 / GRB 101225A: Further NOT optical observation. *GCN Circ.* **11496** (2010)

[40] Wiersema, K., Tanvir, N. R., & Levan, A. J. GRB 101225A: WHT observations. *GCN Circ.* **11502** (2010)

[41] Xu, D. *et al.* GRB 101225A: Host galaxy. *GCN Circ.* **11519** (2011)

[42] Fynbo, J. P. U., & Xu, D. GRB 101225A: Redshift retraction and results of additional photometric follow-up at the NOT. *GCN Circ.* **11563** (2011)

[43] Stritzinger, M. *et al.* Optical photometry of the type Ia supernova 1999ee and the type Ib/c supernova 1999ex in IC 5179. *Astron. J.*, **124**, 2100-2117 (2002)

[44] Galama, T. J. *et al.* An unusual supernova in the error box of the γ-ray burst of 25 April 1998. *Nature*, **395**, 670-672 (1998)

[45] Patat, F. *et al.* The metamorphosis of SN 1998bw. *Astrophys. J.*, **555**, 900-917 (2001)

[46] Anupama, G. C. *et al.* Early time optical spectroscopy of supernova SN 1998S. *Astron.& Astrophys.*, **367**, 506-512 (2001)

[47] Lentz, E. J. *et al.* Analysis of type IIn SN 1998S: effects of circumstellar interaction on observed spectra. *Astrophys. J.*, **547**, 406-411 (2001)

[48] Fassia, A. *et al.* Optical and infrared spectroscopy of the type IIn SN 1998S: days 3-127. *Mon. Not. R. Astron. Soc.*, **325**, 907-930 (2001)

[49] Stoll, R. *et al.* SN 2010jl in UGC 5189: yet another luminous type IIn supernova in a metal-poor galaxy. *Astrophys. J.*, **730**, 34 (10pp) (2011)

[50] Gaskell, C. M. Type II-L supernovae – Standard bombs. *Astrophys. J.*, **389**, L17-L20 (1992)

[51] Leonard, D. C. *et al.* Photospheric-phase spectropolarimetry and nebular-phase spectroscopy of the peculiar Type Ic supernova 2002ap. *Pub. Astron. Soc. Pac.*, **114**, 1333-1348 (2002)

[52] Zeh, A., Klose, S., & Hartmann, D. H., A systematic analysis of supernova light in gamma-ray burst afterglows. *Astrophys. J.*, **609**, 952-961 (2004)

[53] Ferrero, P. *et al.* The GRB 060218/SN 2006aj event in the context of other gamma-ray burst supernovae. *Astron.& Astrophys.*, **457**, 857-864 (2006)

[54] Kann, D. A., Klose, S., & Zeh, A. Signatures of extragalactic dust in pre-Swift GRB afterglows. *Astrophys. J.*, **641**, 993-1009 (2006)

[55] Sollerman, J. *et al.* The nature of the X-ray flash of August 24 2005. Photometric evidence for an on-axis z = 0.83 burst with continuous energy injection and an associated supernova? *Astron.& Astrophys.*, **466**, 839-846 (2007)

[56] Kann, D. A. *et al.* The afterglows of Swift-era gamma-ray bursts. II. Type I GRB versus Type II GRB optical afterglows. *Astrophys. J.*, **734**, 96 (47pp) (2011)

[57] Bloom, J. S. *et al.* Observations of the naked-eye GRB 080319B: implications of nature's brightest explosion *Astrophys. J.*, **691**, 723-737 (2009)

[58] Campana, S. *et al.* Tentative redshift of GRB101225A (Christmas's burst) from Swift-XRT data. *GCN Circ.* **11501** (2010)

[59] Valenti, S. *et al.* A low-energy core-collapse supernova without a hydrogen envelope. *Nature*, **459**, 674-677 (2009)

[60] Roming, P. W. A. *et al.* The first Swift Ultraviolet/Optical Telescope GRB afterglow catalog. *Astrophys. J.*, **690**, 163-188 (2009)

[61] Arnett, W. D. Analytic solutions for light curves of supernovae of Type II. *Astrophys. J.*, **237**, 541-549 (1980)

[62] Kulkarni, S.R. Modeling supernova-like explosions associated with gamma-ray bursts with short durations. *ArXiv e-prints, arXiv:astro-ph/0510256* (2005)

[63] Huang, Y. F., Gou, L. J., Dai, Z. G., & Lu, T. Overall evolution of jetted gamma-ray burst ejecta. *Astrophys. J.*, **543**, 90-96 (2000)